ACS NANO

Cite This: ACS Nano 2018, 12, 8029–8036

www.acsnano.org

ARTICLE

Crystalline Cyclophane–Protein Cage Frameworks

Ngong Kodiah Beyeh,[†,‡,§] Nonappa,[†] Ville Liljeström,[†] Joona Mikkilä,[∥] Antti Korpi,[∥] Davide Bochicchio,[⊥] Giovanni M. Pavan,[⊥] Olli Ikkala,[†] Robin H. A. Ras,[†,∥] and Mauri A. Kostiainen*[,†,∥]

[†]HYBER Centre of Excellence, Department of Applied Physics, Aalto University, FI-00076 Aalto, Finland

[‡]Department of Chemistry and Biochemistry, University of Windsor, N9B 3P4 Windsor, Canada

[§]Department of Chemistry, Oakland University, 146 Library Drive, Rochester, Michigan 48309-4479, United States

[∥]Department of Bioproducts and Biosystems, Aalto University, FI-00076 Aalto, Finland

[⊥]Department of Innovative Technologies, University of Applied Sciences and Arts of Southern Switzerland, CH-6928 Manno, Switzerland

Supporting Information

ABSTRACT: **Cyclophanes are macrocyclic supramolecular hosts famous for their ability to bind atomic or molecular guests *via* noncovalent interactions within their well-defined cavities. In a similar way, porous crystalline networks, such as metal–organic frameworks, can create microenvironments that enable controlled guest binding in the solid state. Both types of materials often consist of synthetic components, and they have been developed within separate research fields. Moreover, the use of biomolecules as their structural units has remained elusive. Here, we have synthesized a library of organic cyclophanes and studied their electrostatic self-assembly with biological metal-binding protein cages (ferritins) into ordered structures. We show that cationic pillar[5]arenes and ferritin cages form biohybrid cocrystals with an open protein network structure. Our cyclophane–protein cage frameworks bridge the gap between molecular frameworks and colloidal nanoparticle crystals and combine the versatility of synthetic supramolecular hosts with the highly selective recognition properties of biomolecules. Such host–guest materials are interesting for porous material applications, including water remediation and heterogeneous catalysis.**

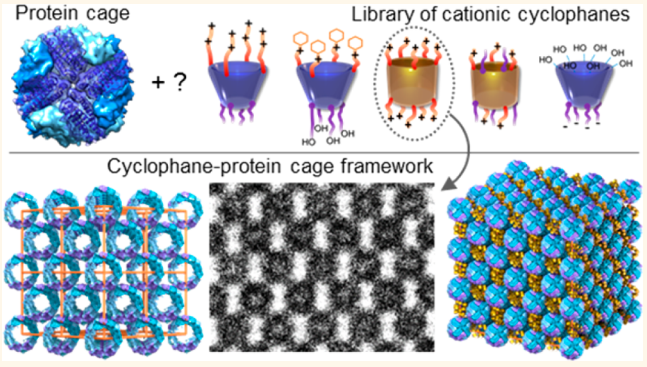

KEYWORDS: *protein cage, cyclophane, pillararene, crystal, self-assembly, electrostatic binding*

Supramolecular materials rely often on macrocycles, such as cyclophanes consisting of aromatic rings and aliphatic carbons, to achieve host–guest chemistry.[1] Calixarenes[2] and pillararenes[3] are well-known cyclophanes, capable of forming cup- and barrel-shaped cavities, respectively. Their ability to bind various small molecular guests is well-established and can be tuned through synthetic modifications. In particular, the guest binding of pillararene hosts changes dramatically when the number or OH group substitution of the hydroquinone units is modified.[4] This variability has made pillararenes relevant to applications, for example, in rapid removal of organic micropollutants from water,[5] host–guest complexation of drug molecules,[6] all-solid-state lithium batteries,[7] and artificial membrane channels.[8]

The cavity type of the materials can be further modified by arranging the building blocks into crystalline networks.[9] Metal–organic frameworks (MOFs) are a classic example that can achieve very high surface area and uptake of various gases,[10] (chiral) catalysts,[11] or even a large biomolecular guest such as proteins and DNA.[12−15] Furthermore, pillararenes have been crystallized into porous structures alone[16] or together with MOFs[17] to form highly porous structures that can be used, for example, to molecularly sort alkanes.[18] Beyond the small molecular host, colloidal nanoparticle supraspheres can be organized into higher-order structures. Their interparticle voids can be several nanometers in diameter and have recently been demonstrated to efficiently take up hydrophobic guest molecules[19] or to reversibly trap molecules for enhanced

Received: April 17, 2018
Accepted: July 13, 2018
Published: July 13, 2018

DOI: 10.1021/acsnano.8b02856
ACS Nano 2018, 12, 8029–8036

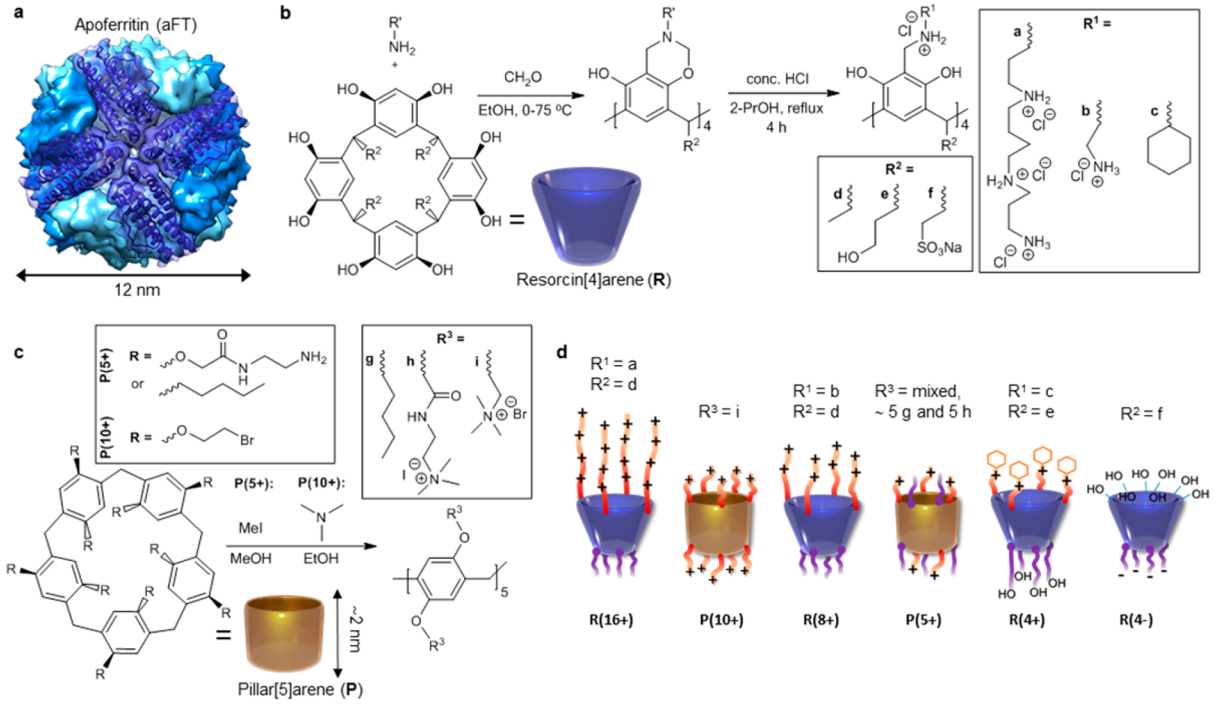

Figure 1. Apoferritin and supramolecular hosts used for the crystal preparation. (a) Recombinant apoferritin from *Pyrococcus furiosus* (PDB id: 2JD6) with a diameter of ~12 nm. (b) Synthesis of the charged resorcin[4]arene (R) hosts. (c) Synthesis of the cationic pillar[5]arene (P) hosts. (d) Schematic presentation of all the hosts used in this study. Diameters (d_{host}) of the cationic hosts are approximately 1.5−2 nm.

reactivity and stereoselectivity.[20] Incorporating MOFs into a mesoporous structure can further improve mass diffusion properties of the material, which highlights the importance of hierarchical frameworks in single-crystalline form.[21]

The diversity of synthetic host molecules is rich and expanding; however, they are still much less sophisticated than those observed in nature.[22] Naturally occurring protein-based hosts have evolved to carry out highly specific functions.[23] Among these, ferritins are a key class of protein cages that are responsible for the nucleation and storage of elementary iron in living organisms.[24] They have also been shown to function as versatile supramolecular templates for the synthesis of different inorganic materials[25] and encapsulation of active biomolecules.[26] The exactly defined structure of ferritin can also be utilized to prepare large 3D crystal structures using a protein−metal−organic approach[27] or electrostatic interactions.[28,29] An intriguing feature of such structures is that they can be used to direct the formation of nanoparticle superlattices, as placing an inorganic particle inside the cage does not affect its capability to form ordered structures.[30,31] Furthermore, apoferritin single crystals have been utilized for structural characterization of the formation of sub-nanoclusters within the ferritin cage.[32] In general, protein crystals with large voids can function in ways similar to those of other porous structures and host various guests *via* supramolecular interactions.[33−36]

In this article, we present a framework material that combines synthetic cyclophane hosts and native metal-binding protein cages. The advantage is that such an approach offers means to combine different hosts with specific recognition properties. Such materials have been shown to exhibit improved mass diffusion properties, and they enable binding of organic molecules close to catalytically active inorganic centers, which can be used to develop efficient and recyclable catalysts.[21] We describe the synthesis of several cationic cyclophane hosts, consisting of resorcinarenes and pillararenes and show that hosts with more than five protonatable amines can efficiently bind negatively charged apoferritin protein cage particles and form large complexes. When the number and orientation of electrostatic interactions between the host and apoferritin are optimized, the system self-assembles into a porous cyclophane−protein cage framework (CPF). In the case of symmetrically cationic pillar[5]arene with 10 cationic charges, the CPF adopts a crystal structure where the apoferritin forms a face-centered cubic (fcc) lattice, and the pillar[5]arene hosts are electrostatically bridging the protein lattice and occupying the void spaces between the particles.

RESULTS AND DISCUSSION

Apoferritin (aFT) from *Pyrococcus furiosus* was chosen as the protein part due to its well-defined size (diameter ~12 nm), spherical shape, and hollow cavity of ~8 nm. The cage consists of 24 protein subunits with 432 point group symmetry (Figure 1a) and has a total molecular weight of approximately 0.5 MDa.[37] There are eight three-fold and six four-fold channels that span the cage and allow diffusion into the cavity. The cationic resorcin[4]arene hosts were synthesized by reacting the upper rim 2-position of the phenyl group with benzyloxycarbonyl (Boc)-protected amine in the presence of excess formaldehyde in a Mannich condensation reaction.[38,39] Finally, the Boc protection was removed using acid hydrolysis to achieve resorcin[4]arene hosts with 4, 8, and 16 amines (hosts **R(4+)**, **R(8+)**, and **R(16+)**, respectively). Additionally, a negatively charged control resorcinarene **R(4−)** was prepared. The synthesis of pillar[5]arenes with 5 (**P(5+)**) or 10 (**P(10+)**) quaternized amines was carried out by first preparing the macrocycle with either ethyl bromide or with ethylenediamine methyl acetate functionalization and finally

DOI: 10.1021/acsnano.8b02856
ACS Nano 2018, 12, 8029−8036

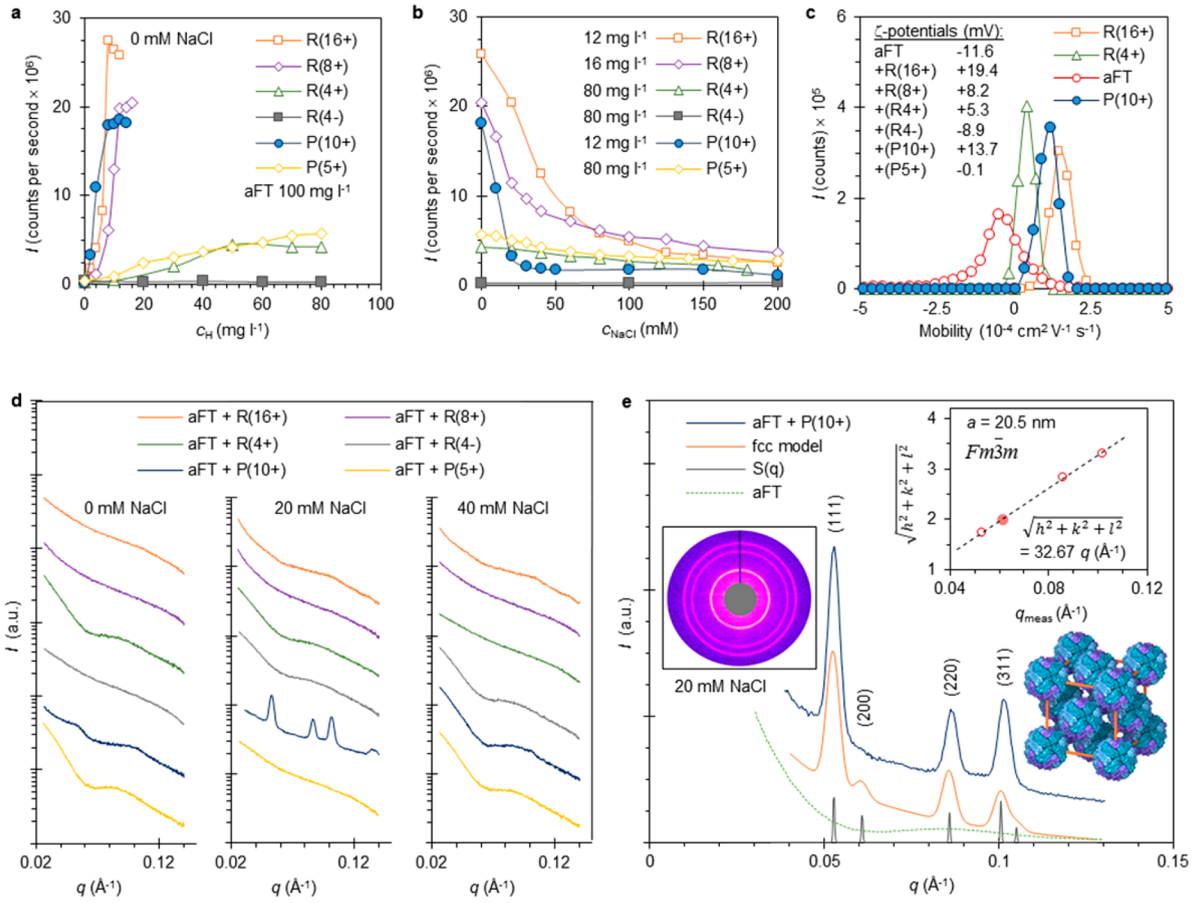

Figure 2. Assembly, disassembly, and crystal structure of aFT−host complexes. (a) aFT solution titrated with different hosts monitored with DLS shows that the highly cationic hosts complex aFT efficiently. (b) End point of the titration in panel a titrated with NaCl shows that the complexes can be disassembled by increasing the electrolyte concentration. (c) Electrophoretic mobility and ζ-potential measured from selected aFT−host complexes. (d) Small-angle X-ray scattering (SAXS) curves measured for the different aFT−host complexes at various electrolyte concentrations. Ordered assemblies are achieved only for the aFT−P(10+) complex at 20 mM NaCl. (e) SAXS data compared to the theoretical fcc scattering structure factor S(q), fitted model, and free aFT (data curves offset in y-direction for clarity). Inset: Miller indices of assigned reflections for the fcc structure *versus* measured q-vector positions for indexed peaks yield unit cell dimensions of a = 20.5 nm (space group $Fm\bar{3}m$, number 225). The (200) peak, which coincides with aFT form factor minimum, is marked with a filled symbol.

converted to quaternary ammonium groups by either trimethylamine (**P(10+)**) or methyl iodide (**P(5+)**) treatment. The key synthesis steps and a schematic presentation of all the prepared cationic hosts are presented in Figure 1b−d, respectively. Full experimental details together with characterization data are given in the Supporting Information section 1 (Schemes S1−S4 and Figures S1−S6).

Initially, the hosts' ability to bind and complex aFT into larger assemblies was studied by following the increase in count rate with dynamic light scattering (DLS). An aqueous solution of aFT (100 mg L^{-1}) was slowly titrated with the host (0−80 mg L^{-1}). The assemblies form almost instantaneously after host addition. Figure 2a presents the titration curves for all host compounds. The hosts with a high number of cationic amines (**R(16+)**, **R(8+)**, and **P(10+)**) were able to fully complex aFT at low concentrations (c_H < 20 mg L^{-1}) as indicated by the rapid increase in the observed count rate and hydrodynamic diameter (to ∼2 μm, Figure S7a). In the case of **P(10+)**, maximum intensity is achieved at 12 mg L^{-1}, which corresponds to approximately 25 hosts per aFT. However, the hosts with an intermediate amount of positive charges ((**R(4+)** and **P(5+)**) were able to bind the aFT but at much higher concentrations (c_H > 50 mg L^{-1}) and lower final count rate. As expected, the negatively charged resorcinarene **R(4−)** was not able to interact efficiently with aFT due to the lack of attractive electrostatic interactions, and consequently, no changes in the count rate were observed.

Because the electrostatic interactions are sensitive to the presence of electrolytes and can be screened by increasing the electrolyte concentrations, we studied how the assemblies are affected by the addition of NaCl (0−200 mM). All complexes could be disassembled by NaCl addition (Figure 2b). In the case of **P(10+)**, the disassembly was more complete than with the other hosts and took place at NaCl concentrations above 30 mM. Full disassembly of these complexes could also be induced by lowering the pH close to the isoelectric point of aFT (∼4.5) or by temperature increase to 60 °C (Figure S8). The resorcinarene host-based assemblies did not disassemble completely at medium 50 mM NaCl concentration, which can be explained by their partial amphiphilic nature and the presence of attractive hydrophobic interactions between the building blocks. At 200 mM NaCl concentration, the complexes are almost fully disassembled and free aFT particles are mostly observed (Figure S7b). Electrophoretic mobility and ζ-potential (ζp) measurements presented in Figure 2c verify the overall negative charge of the free aFT particles (ζp

DOI: 10.1021/acsnano.8b02856
ACS Nano 2018, 12, 8029−8036

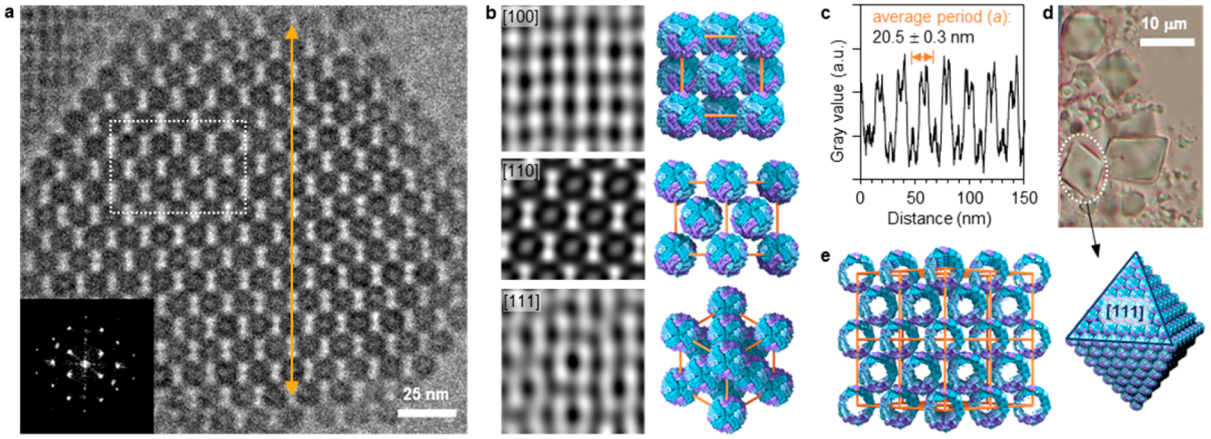

Figure 3. Cryo-TEM and optical microscopy imaging of the crystals. (a) Cryo-TEM image of vitrified aqueous solution containing a crystal viewed along the [110] projection axis. Inset: Fast Fourier transform (FFT). The area marked by the dotted white line is presented schematically in panel e. (b) Inverse and filtered FFT with selected Fourier components from images viewing crystals along [100] (top), [110] (middle), and [111] (bottom) projection axes (left) as well as comparison to a unit cell viewed along the given projection axes (right). (c) Integrated profile along the orange line in panel a, yielding an aFT center-to-center distance of 20.5 nm. (d) Crystals with octahedral habit and sizes over 10 μm observed with an optical microscope (top). A model of fcc-packed aFT cages with octahedral shape and highlighted [111] face (bottom). (e) Image of the 2 × 2 unit cell demonstrates the highly porous structure of the protein cage crystal. aFT is shown as a ring (center slice) to illustrate the hollow cavity.

= −11.6 mV). The complexes have clearly a lower negative charge, and again, the highest charge can be associated with the assemblies that are formed with the highest number of protonatable amines (see Figure S7c for all mobility data). For the **R(16+)**-, **R(8+)**-, and **P(10+)**-based assemblies, ζp values of >10 mV are routinely observed.

We then turned to the formation of ordered CPF structures from aFT and the prepared hosts. We have previously shown that the electrostatic attraction in such systems must be carefully controlled if crystalline assemblies are to be formed.[31] At low electrolyte concentration, the oppositely charged building blocks are strongly attracted to each other, and consequently, kinetically trapped systems with the lack of long-range order form easily.[40] The attraction must be pushed into a weak regime (few k_BT) by increasing the electrolyte concentration that modulates the electrostatic interactions. Increasing the electrolyte concentration too much screens the attractive interactions and prevents assembly formation almost entirely, as already shown by the DLS data. All hosts were therefore assembled with aFT in a range of different NaCl concentrations (0−40 mM) and studied by small-angle X-ray scattering (SAXS) to estimate the degree of crystallinity. Surprisingly, none of the resorcinarene hosts could assemble to ordered frameworks with aFT even when thoroughly optimized. Only the **P(10+)** was able to form ordered structures at 20 mM NaCl concentration, as indicated by the clear Bragg reflections (Figure 2d). Again, the alkyl chains on the lower rim of the resorcinarene hosts can provide additional attractive hydrophobic interactions, which cannot be screened by the electrolyte addition, resulting in poorly ordered assemblies. The less charged hosts, including the **P(5+)**, cannot provide sufficient interactions to yield large ordered assemblies.

The 2D scattering pattern measured directly from a solution of aFT−**P(10+)** crystals shows clear Debye rings, which indicate the presence of multiple crystals with isotropic orientation. Such patterns are often measured from powder-like samples and are typical of polycrystalline morphology. The intensity maxima are found from the azimuthally integrated curve at q_{hkl} = 0.053, 0.086, and 0.102 Å^{-1} (Figure 2e). The relative peak positions (q_{hkl}/q^*, here q^* = 0.0306 Å^{-1}) indicate an fcc lattice as they coincide with the first allowed reflections of an fcc lattice, which are the (111), (200), (220), and (311) reflections found at $q_{hkl}/q^* = \sqrt{3}$, $\sqrt{4}$, $\sqrt{8}$, and $\sqrt{11}$, respectively. The (200) peak coincides with the form factor minimum of the aFT, which explains why it is only weakly detectable at ∼0.061 Å^{-1}. The lattice constant a_{SAXS} was estimated from the SAXS data by plotting the quadratic Miller indices against the measured q values (Figure 2e inset). A linear regression yielded $\sqrt{(h^2 + k^2 + l^2)} = 32.67\ q$ (Å^{-1}), and for the observed fcc lattice, $a_{SAXS} = 2\pi \times 32.67$ Å = 20.5 nm. The comparison to a simulated scattering curve from a finite fcc model and the corresponding structure factor ($S(q)$) confirms the $Fm\bar{3}m$ Bravais lattice space group (number 225). The calculated nearest neighbor aFT center-to-center distance is 14.5 nm, which leaves a ∼2.5 nm space between the adjacent aFT particles. These dimensions correspond well with the size of the aFT cage (d_{aFT} ∼ 12 nm) separated by the **P(10+)** host (d_{host} ∼ 1.5 nm).

To visualize and further analyze the formed lattices, we turned to cryogenic transmission electron microscopy (cryo-TEM). A vitrified sample from the freshly prepared solution of the crystals was imaged at 300 kV acceleration voltage. Figure 3a shows a typical small crystallite viewed along the [110] projection axis. The highly ordered arrangement of individual aFT particles is clearly visible. Low-magnification images showing multiple highly ordered complexes from random orientations of the lattices are presented in the Supporting Information (Figure S9). From these images, it is possible to find all the expected projections of the fcc lattice. Figure 3b shows the filtered inverse Fourier transform from selected Fourier components of lattice projections viewed along [100], [110], and [111] projection axes. The observed images match closely with the expected projections of the model unit cell. Measuring the dimensions of the lattice along the [110] projection yields a lattice constant, a_{TEM} = 20.5 nm, which matches exactly with the SAXS data.

DOI: 10.1021/acsnano.8b02856
ACS Nano 2018, 12, 8029−8036

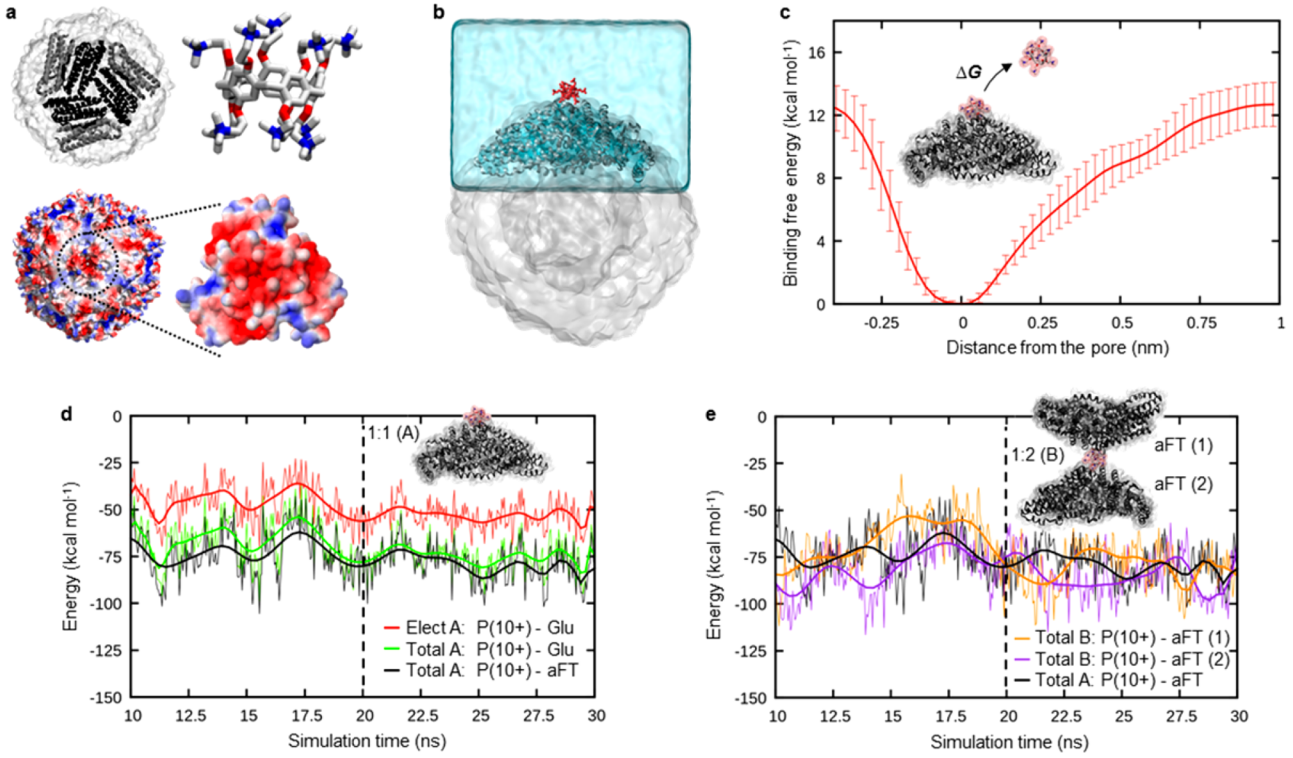

Figure 4. Atomistic simulation of P(10+) binding to aFT. (a) Atomistic model of aFT and P(10+) (top) and electrostatic potential for aFT (bottom). Calculated crude vacuum electrostatic potential of the full cages (left) and solution electrostatic surface potential of protein trimer subunits (right) are presented. Red and blue colors represent negative and positive electrostatic potential, respectively. Values range from 0 $k_BT\ e^{-1}$ (blue) to −9 $k_BT\ e^{-1}$ (red), where k_B is Boltzmann's constant, T is absolute temperature, and e is elementary charge. (b) Atomistic system used to model the molecular recognition between aFT (a portion of the aFT cage containing one negatively charged pore) and one P(10+) molecule *via* MD simulation in explicit solvent. (c) Binding free energy (ΔG) profile as a function of distance from the pore for one P(10+) to one aFT pore in explicit water (inset) obtained from four independent metadynamics simulations. The free energy minimum, corresponding to the bound state, has been set to zero. (d) Interaction energies extracted from the MD simulations. The last 10 ns of MD simulations are representative of the equilibrium. Nonbonded interaction energies in the system with one aFT portion and one P(10+): electrostatic interaction energy (Elect) between P(10+) and Glu amino acids (red) as well as total nonbond interaction energy (electrostatic + van der Waals) (green), and total interaction energy between P(10+) and aFT (black). (e) Comparison of the total nonbonded interaction energies in the systems A (one P(10+) and one aFT, black) and B (one P(10+) and two aFT, orange and purple for aFT (1) and aFT (2)); the interaction energies are of similar strength.

The relation between the crystal structure and crystal habit can be directly observed when imaging the crystals with optical microscopy. During growth, the crystals develop a clear octahedral habit (Figure 3d), and the dimensions of the crystal can easily be >10 μm (Figure S10a). aFT crystallization has been observed to proceed in the {111} lattice plane by the formation of step edges.[41] Also in the case aFT−**P(10+)** crystals, the surface energy is presumably smallest for the close-packed {111} faces, and growth of these eight faces leads to the observed octahedral habit (Figure S10b,c). The structure contains large cavities (Figure 3e), where the largest octahedral and tetrahedral voids are 8.5 and 5.8 nm in diameter, respectively. By assuming a spherical aFT particle with an inner hollow core, the space not occupied by ferritin protein subunits is very large and consists of approximately 66% of the volume of the unit cell (Figure S11). This shows that the structure has a percolated network of large voids between the aFT particles that can be occupied by the **P(10+)** hosts.

To obtain an insight into the interactions between **P(10+)** and aFT, we used molecular dynamics simulations. First, an atomistic model for both interacting species (Figure 4a, top) was created. Analysis of the electrostatic potential of the aFT cage surface revealed that it has a net negative charge. There are several negatively charged patches, but most of the negative charge of ferritin is located around the pores present at the three-fold symmetry axes, which constitute potential binding sites for the positively charged **P(10+)** (Figure 4a, bottom). However, binding to the other negatively charged patches can most likely also take place in this system. The large size of aFT prevents atomistic simulation of the full cage. Thus, as recently done to study the interaction of positively charged binders with viral capsids[42] and microtubules,[43] we first focused on the study of the local binding between one **P(10+)** and one three-fold binding site on the aFT cage. We cut a portion of the cage constituted by the protein chains surrounding the pore (Figure 4b, black α-helices) and their closest neighbors (gray). One **P(10+)** molecule was then placed in close vicinity above the pore and was observed to bind and equilibrate onto the cage pore by means of unbiased all-atom molecular dynamics (AA-MD) simulation in explicit water and ions (Figure 4b). Full computational details are provided in the Methods section and in the Supporting Information (Table S1). Metadynamics simulations (Figure 4c) then allowed us to quantify the free energy of binding of **P(10+)** to the cage pore as $\Delta G = -13 \pm 1.4$ kcal mol^{-1} (average ± standard error). Analysis of the nonbond interactions conducted on the unbiased AA-MD trajectories (Figure 4d) indicated that the **P(10+)** binding is controlled by favorable interactions with negatively charged

DOI: 10.1021/acsnano.8b02856
ACS Nano 2018, 12, 8029−8036

glutamate (Glu) amino acids (Glu 109/121), particularly dense in the pore region (capturing ∼96% of the total nonbond interaction with the surface). Of this interaction with Glu residues, ∼70% is controlled by electrostatic interactions (Figure 4d).

Next, starting from the equilibrated 1:1 **P(10+)**−aFT obtained from AA-MD, we built another molecular model containing a second cage pore region symmetrically bound to the same binder (Figure 4e, 1:2 system). This model was equilibrated in explicit water and counterions by means of AA-MD simulation, providing information on the interactions of **P(10+)** bridging two cages. The extracted data demonstrated that a single **P(10+)** can stably interact with two cages. From this AA-MD simulation, we could observe that the interaction is symmetric, indicating that the binding to a second cage does not impair the binding to the first one.

CONCLUSION

We have laid out the rules for preparing framework materials from synthetic cyclophanes and protein cages. A facially symmetric pillar[5]arene with 10 protonatable amines was identified as the optimal host to electrostatically self-assemble with ferritin cages to yield ordered framework structures. The crystals have large interconnected voids between the protein cages that are in the size range of several nanometers. We envision that following the presented design parameters, it is possible to prepare CPFs from a variety of cyclophanes and tune the binding properties of the resulting framework materials. Furthermore, it would be possible to expand the design space of CPFs by using *de novo* engineered protein cages.[44−46] These developments could in the future lead to an efficient heterogeneous catalyst, where the cyclophanes are able to trap guest molecules close to the catalytic sites of the biomolecules,[20] multifunctional water remediation materials,[47] or preparation of zeolite-type structures with rod-like biomolecules.[48]

METHODS

Dynamic Light Scattering and ζ-Potential Measurements. The hydrodynamic diameter (D_h) of the assemblies was measured using a Malvern Instruments DLS device (Zetasizer Nano ZS Series) with a 4 mW He−Ne ion laser at a wavelength of 633 nm and an avalanche photodiode detector at an angle of 173°. Experiments were carried out at 25 °C. Plastibrand semimicro poly(methyl methacrylate) cuvettes and Malvern disposable ζ-cells were used for the size and electrophoretic mobility measurements, respectively. Zetasizer software (Malvern Instruments) was used to obtain the particle size distributions and ζ-potentials.

Cryogenic Transmission Electron Microscopy. The cryo-TEM images were collected using JEM 3200FSC field emission microscope (JEOL) operated at 300 kV in bright-field mode with Omega-type zero-loss energy filter. The images were acquired with Gatan digital micrograph software, and the specimen temperature was maintained at −187 °C. The cryo-TEM samples were prepared by placing 3 μL of a freshly prepared aqueous dispersion of the sample on a 200 mesh copper grid with holey carbon support film (CF-Quantifoil) and plunge-freezed using Vitrobot with 3 s blotting time under 100% humidity. The TEM grids were plasma-cleaned using a Gatan Solarus (model 950) plasma cleaner for 30 s before placing the sample.

Small-Angle X-ray Scattering. The aqueous samples were sealed between two Kapton foils inside a metal washer. The sample environment was evacuated to reduce background scattering from air. The SAXS was measured using a Bruker Microstar microfocus rotating anode X-ray source (Cu Kα radiation, λ = 1.54 Å). The beam was monochromated and focused by a Montel multilayer focusing monochromator (Incoatec). The X-ray beam was further collimated by four collimation slits (JJ X-ray), resulting in a final spot size of less than 1 mm at the sample position. A Hi-Star 2D area detector (Bruker) was used to collect the scattered intensity. Sample-to-detector distance was 1.59 m, and a silver behenate standard sample was used for the calibration of the length of the scattering vector q. One-dimensional SAXS data were obtained by azimuthally averaging the 2D scattering data, and the magnitude of the scattering vector q is given by $q = 4\pi \sin\theta/\lambda$, where 2θ is the scattering angle.

Sample Preparation for SAXS, Cryo-TEM, and Optical Microscopy. Cyclophane−aFT samples were prepared by combining 6 μL of aqueous aFT solution (15 mg mL^{-1}, *Pyrococcus furiosus*, Molecular Links Rome), 3.5 μL 20 mM Tris pH 8.5 buffer, 1.5 μL of 0−400 mM NaCl solution, and 4 μL of 10 mg mL^{-1} cyclophane in water, in this order. The samples were gently mixed with a pipet and allowed to set.

All-Atom Simulations. All simulations were conducted using the GROMACS 5.1.2 software and the PLUMED 2 plugin.[49,50] The atomistic model for **P(10+)** was parametrized with the general Amber force field, and aFT was parametrized using the Amber force field *ff12SB*. The **P(10+)** binding energy (ΔG) was calculated from metadynamics simulations. All computational details on the creation of the molecular systems, their equilibration, and the simulation parameters used in AA-MD and metadynamics simulations are provided in the Supporting Information.

ASSOCIATED CONTENT

Supporting Information

The Supporting Information is available free of charge on the ACS Publications website at DOI: 10.1021/acsnano.8b02856.

Details of the synthesis, full experimental methods, additional DLS and TEM analysis (PDF)

AUTHOR INFORMATION

Corresponding Author

*E-mail: mauri.kostiainen@aalto.fi.

ORCID

Ngong Kodiah Beyeh: 0000-0003-3935-1812
Nonappa: 0000-0002-6804-4128
Davide Bochicchio: 0000-0002-3682-9086
Giovanni M. Pavan: 0000-0002-3473-8471
Olli Ikkala: 0000-0002-0470-1889
Robin H. A. Ras: 0000-0002-2076-242X
Mauri A. Kostiainen: 0000-0002-8282-2379

Notes

The authors declare no competing financial interest.

ACKNOWLEDGMENTS

Financial support from the Academy of Finland (Grants 308578, 303804, 273645, 267497, and 272579), Walter Ahlström Foundation, Finnish Cultural Foundation, and Sigrid Juselius Foundation are gratefully acknowledged. D.B. and G.M.P. acknowledge the Swiss National Science Foundation (SNSF Grant 200021_175735 to G.M.P.). This work was carried out under the Academy of Finland's Centers of Excellence Programme and made use of the Aalto University Nanomicroscopy Centre (Aalto NMC) and Bioeconomy Infrastructure. The authors thank Prof. K. Rissanen for discussions and support.

REFERENCES

(1) Liu, Z.; Nalluri, S. K. M.; Stoddart, J. F. Surveying Macrocyclic Chemistry: From Flexible Crown Ethers to Rigid Cyclophanes. *Chem. Soc. Rev.* **2017**, *46*, 2459−2478.

DOI: 10.1021/acsnano.8b02856
ACS Nano 2018, 12, 8029−8036

(2) Böhmer, V. Calixarenes, Macrocycles with (Almost) Unlimited Possibilities. *Angew. Chem., Int. Ed. Engl.* **1995**, *34*, 713−745.
(3) Xue, M.; Yang, Y.; Chi, X.; Zhang, Z.; Huang, F. Pillararenes, a New Class of Macrocycles for Supramolecular Chemistry. *Acc. Chem. Res.* **2012**, *45*, 1294−1308.
(4) Ogoshi, T.; Yamagishi, T.; Nakamoto, Y. Pillar-Shaped Macrocyclic Hosts Pillar[n]arenes: New Key Players for Supramolecular Chemistry. *Chem. Rev.* **2016**, *116*, 7937−8002.
(5) Shi, B.; Guan, H.; Shangguan, L.; Wang, H.; Xia, D.; Kong, X.; Huang, F. A Pillar[5]arene-Based 3D Network Polymer for Rapid Removal of Organic Micropollutants from Water. *J. Mater. Chem. A* **2017**, *5*, 24217−24222.
(6) Wheate, N. J.; Dickson, K.-A.; Kim, R. R.; Nematollahi, A.; Macquart, R. B.; Kayser, V.; Yu, G.; Church, W. B.; Marsh, D. J. Host-Guest Complexes of Carboxylated Pillar[n]arenes with Drugs. *J. Pharm. Sci.* **2016**, *105*, 3615−3625.
(7) Zhu, Z.; Hong, M.; Guo, D.; Shi, J.; Tao, Z.; Chen, J. All-Solid-State Lithium Organic Battery with Composite Polymer Electrolyte and Pillar[5]quinone Cathode. *J. Am. Chem. Soc.* **2014**, *136*, 16461−16464.
(8) Hu, X.-B.; Chen, Z.; Tang, G.; Hou, J.-L.; Li, Z.-T. Single-Molecular Artificial Transmembrane Water Channels. *J. Am. Chem. Soc.* **2012**, *134*, 8384−8387.
(9) Inokuma, Y.; Kawano, M.; Fujita, M. Crystalline Molecular Flasks. *Nat. Chem.* **2011**, *3*, 349−358.
(10) Furukawa, H.; Ko, N.; Go, Y. B.; Aratani, N.; Choi, S. B.; Choi, E.; Yazaydin, A. Ö.; Snurr, R. Q.; O'Keeffe, M.; Kim, J.; Yaghi, O. M. Ultrahigh Porosity in Metal-Organic Frameworks. *Science* **2010**, *329*, 424−428.
(11) Ma, L.; Falkowski, J. M.; Abney, C.; Lin, W. A Series of Isoreticular Chiral Metal−Organic Frameworks as a Tunable Platform for Asymmetric Catalysis. *Nat. Chem.* **2010**, *2*, 838−846.
(12) Maurin, G.; Serre, C.; Cooper, A.; Férey, G. The New Age of MOFs and of Their Porous-Related Solids. *Chem. Soc. Rev.* **2017**, *46*, 3104−3107.
(13) Feng, D.; Liu, T.-F.; Su, J.; Bosch, M.; Wei, Z.; Wan, W.; Yuan, D.; Chen, Y.-P.; Wang, X.; Wang, K.; Lian, X.; Gu, Z.-Y.; Park, J.; Zou, X.; Zhou, H.-C. Stable Metal-Organic Frameworks Containing Single-Molecule Traps for Enzyme Encapsulation. *Nat. Commun.* **2015**, *6*, 5979.
(14) Sontz, P. A.; Bailey, J. B.; Ahn, S.; Tezcan, F. A. A Metal Organic Framework with Spherical Protein Nodes: Rational Chemical Design of 3D Protein Crystals. *J. Am. Chem. Soc.* **2015**, *137*, 11598−11601.
(15) Liang, K.; Ricco, R.; Doherty, C. M.; Styles, M. J.; Bell, S.; Kirby, N.; Mudie, S.; Haylock, D.; Hill, A. J.; Doonan, C. J.; Falcaro, P. Biomimetic Mineralization of Metal-Organic Frameworks as Protective Coatings for Biomacromolecules. *Nat. Commun.* **2015**, *6*, 7240.
(16) Ogoshi, T.; Sueto, R.; Yoshikoshi, K.; Sakata, Y.; Akine, S.; Yamagishi, T. Host-Guest Complexation of Perethylated Pillar[5]-arene with Alkanes in the Crystal State. *Angew. Chem., Int. Ed.* **2015**, *54*, 9849−9852.
(17) Strutt, N. L.; Fairen-Jimenez, D.; Iehl, J.; Lalonde, M. B.; Snurr, R. Q.; Farha, O. K.; Hupp, J. T.; Stoddart, J. F. Incorporation of an A1/A2-Difunctionalized Pillar[5]arene into a Metal−Organic Framework. *J. Am. Chem. Soc.* **2012**, *134*, 17436−17439.
(18) Ogoshi, T.; Sueto, R.; Hamada, Y.; Doitomi, K.; Hirao, H.; Sakata, Y.; Akine, S.; Kakuta, T.; Yamagishi, T. Alkane-Length Sorting Using Activated Pillar[5]arene Crystals. *Chem. Commun.* **2017**, *53*, 8577−8580.
(19) Wang, Y.; Zeiri, O.; Raula, M.; Le Ouay, B.; Stellacci, F.; Weinstock, I. A. Host−Guest Chemistry with Water-Soluble Gold Nanoparticle Supraspheres. *Nat. Nanotechnol.* **2016**, *12*, 170−176.
(20) Zhao, H.; Sen, S.; Udayabhaskararao, T.; Sawczyk, M.; Kučanda, K.; Manna, D.; Kundu, P. K.; Lee, J.-W.; Král, P.; Klajn, R. Reversible Trapping and Reaction Acceleration within Dynamically Self-Assembling Nanoflasks. *Nat. Nanotechnol.* **2015**, *11*, 82−88.
(21) Shen, K.; Zhang, L.; Chen, X.; Liu, L.; Zhang, D.; Han, Y.; Chen, J.; Long, J.; Luque, R.; Li, Y.; Chen, B. Ordered Macro-Microporous Metal-Organic Framework Single Crystals. *Science* **2018**, *359*, 206−210.
(22) Douglas, T.; Young, M. Host-Guest Encapsulation of Materials by Assembled Virus Protein Cages. *Nature* **1998**, *393*, 152−155.
(23) Uchida, M.; Klem, M. T.; Allen, M.; Suci, P.; Flenniken, M.; Gillitzer, E.; Varpness, Z.; Liepold, L. O.; Young, M.; Douglas, T. Biological Containers: Protein Cages as Multifunctional Nanoplatforms. *Adv. Mater.* **2007**, *19*, 1025−1042.
(24) Harrison, P. M.; Arosio, P. The Ferritins: Molecular Properties, Iron Storage Function and Cellular Regulation. *Biochim. Biophys. Acta, Bioenerg.* **1996**, *1275*, 161−203.
(25) Uchida, M.; Kang, S.; Reichhardt, C.; Harlen, K.; Douglas, T. The Ferritin Superfamily: Supramolecular Templates for Materials Synthesis. *Biochim. Biophys. Acta, Gen. Subj.* **2010**, *1800*, 834−845.
(26) Tetter, S.; Hilvert, D. Enzyme Encapsulation by a Ferritin Cage. *Angew. Chem., Int. Ed.* **2017**, *56*, 14933−14936.
(27) Bailey, J. B.; Zhang, L.; Chiong, J. A.; Ahn, S.; Tezcan, F. A. Synthetic Modularity of Protein−Metal−Organic Frameworks. *J. Am. Chem. Soc.* **2017**, *139*, 8160−8166.
(28) Mikkilä, J.; Anaya-Plaza, E.; Liljeström, V.; Caston, J. R.; Torres, T.; De La Escosura, A.; Kostiainen, M. A. Hierarchical Organization of Organic Dyes and Protein Cages into Photoactive Crystals. *ACS Nano* **2016**, *10*, 1565−1571.
(29) Liljeström, V.; Seitsonen, J.; Kostiainen, M. A. Electrostatic Self-Assembly of Soft Matter Nanoparticle Cocrystals with Tunable Lattice Parameters. *ACS Nano* **2015**, *9*, 11278−11285.
(30) Künzle, M.; Eckert, T.; Beck, T. Binary Protein Crystals for the Assembly of Inorganic Nanoparticle Superlattices. *J. Am. Chem. Soc.* **2016**, *138*, 12731−12734.
(31) Kostiainen, M. A.; Hiekkataipale, P.; Laiho, A.; Lemieux, V.; Seitsonen, J.; Ruokolainen, J.; Ceci, P. Electrostatic Assembly of Binary Nanoparticle Superlattices Using Protein Cages. *Nat. Nanotechnol.* **2013**, *8*, 52−56.
(32) Maity, B.; Abe, S.; Ueno, T. Observation of Gold Sub-Nanocluster Nucleation within a Crystalline Protein Cage. *Nat. Commun.* **2017**, *8*, 14820.
(33) Abe, S.; Tabe, H.; Ijiri, H.; Yamashita, K.; Hirata, K.; Atsumi, K.; Shimoi, T.; Akai, M.; Mori, H.; Kitagawa, S.; Ueno, T. Crystal Engineering of Self-Assembled Porous Protein Materials in Living Cells. *ACS Nano* **2017**, *11*, 2410−2419.
(34) Abe, S.; Maity, B.; Ueno, T. Design of a Confined Environment Using Protein Cages and Crystals for the Development of Biohybrid Materials. *Chem. Commun.* **2016**, *52*, 6496−6512.
(35) Tabe, H.; Fujita, K.; Abe, S.; Tsujimoto, M.; Kuchimaru, T.; Kizaka-Kondoh, S.; Takano, M.; Kitagawa, S.; Ueno, T. Preparation of a Cross-Linked Porous Protein Crystal Containing Ru Carbonyl Complexes as a CO-Releasing Extracellular Scaffold. *Inorg. Chem.* **2015**, *54*, 215−220.
(36) Liljeström, V.; Mikkilä, J.; Kostiainen, M. A. Self-Assembly and Modular Functionalization of Three-Dimensional Crystals from Oppositely Charged Proteins. *Nat. Commun.* **2014**, *5*, 4445.
(37) Tatur, J.; Hagen, W. R.; Matias, P. M. Crystal Structure of the Ferritin from the Hyperthermophilic Archaeal Anaerobe *Pyrococcus furiosus*. *JBIC, J. Biol. Inorg. Chem.* **2007**, *12*, 615−630.
(38) Iwanek, W.; Mattay, J. Chiral Calixarenes Derived from Resorcinol. *Liebigs Ann. Chem.* **1995**, *1995*, 1463−1466.
(39) Beyeh, N. K.; Jo, H. H.; Kolesnichenko, I.; Pan, F.; Kalenius, E.; Anslyn, E. V.; Ras, R. H. A.; Rissanen, K. Recognition of Viologen Derivatives in Water by *N*-Alkyl Ammonium Resorcinarene Chlorides. *J. Org. Chem.* **2017**, *82*, 5198−5203.
(40) Velev, O. D. Self-Assembly of Unusual Nanoparticle Crystals. *Science* **2006**, *312*, 376−377.
(41) Yau, S. T.; Vekilov, P. G. Quasi-Planar Nucleus Structure in Apoferritin Crystallization. *Nature* **2000**, *406*, 494−497.
(42) Doni, G.; Kostiainen, M. A.; Danani, A.; Pavan, G. M. Generation-Dependent Molecular Recognition Controls Self-Assem-

DOI: 10.1021/acsnano.8b02856
ACS Nano 2018, 12, 8029−8036

bly in Supramolecular Dendron-Virus Complexes. *Nano Lett.* **2011**, *11*, 723−728.
(43) Garzoni, M.; Okuro, K.; Ishii, N.; Aida, T.; Pavan, G. M. Structure and Shape Effects of Molecular Glue on Supramolecular Tubulin Assemblies. *ACS Nano* **2014**, *8*, 904−914.
(44) Lai, Y.-T.; Reading, E.; Hura, G. L.; Tsai, K.-L.; Laganowsky, A.; Asturias, F. J.; Tainer, J. A.; Robinson, C. V.; Yeates, T. O. Structure of a Designed Protein Cage That Self-Assembles into a Highly Porous Cube. *Nat. Chem.* **2014**, *6*, 1065−1071.
(45) Fletcher, J. M.; Harniman, R. L.; Barnes, F. R. H.; Boyle, A. L.; Collins, A.; Mantell, J.; Sharp, T. H.; Antognozzi, M.; Booth, P. J.; Linden, N.; Miles, M. J.; Sessions, R. B.; Verkade, P.; Woolfson, D. N. Self-Assembling Cages from Coiled-Coil Peptide Modules. *Science* **2013**, *340*, 595−599.
(46) Hsia, Y.; Bale, J. B.; Gonen, S.; Shi, D.; Sheffler, W.; Fong, K. K.; Nattermann, U.; Xu, C.; Huang, P.-S.; Ravichandran, R.; Yi, S.; Davis, T. N.; Gonen, T.; King, N. P.; Baker, D. Design of a Hyperstable 60-Subunit Protein Icosahedron. *Nature* **2016**, *535*, 136−139.
(47) Alsbaiee, A.; Smith, B. J.; Xiao, L.; Ling, Y.; Helbling, D. E.; Dichtel, W. R. Rapid Removal of Organic Micropollutants from Water by a Porous β-Cyclodextrin Polymer. *Nature* **2016**, *529*, 190−194.
(48) Liljeström, V.; Ora, A.; Hassinen, J.; Rekola, H. T.; Nonappa; Heilala, M.; Hynninen, V.; Joensuu, J. J.; Ras, R. H. A.; Törmä, P.; Ikkala, O.; Kostiainen, M. A. Cooperative Colloidal Self-Assembly of Metal-Protein Superlattice Wires. *Nat. Commun.* **2017**, *8*, 671.
(49) Abraham, M. J.; Murtola, T.; Schulz, R.; Páll, S.; Smith, J. C.; Hess, B.; Lindahl, E. GROMACS: High Performance Molecular Simulations through Multi-Level Parallelism from Laptops to Supercomputers. *SoftwareX* **2015**, *1−2*, 19−25.
(50) Tribello, G. A.; Bonomi, M.; Branduardi, D.; Camilloni, C.; Bussi, G. PLUMED 2: New Feathers for an Old Bird. *Comput. Phys. Commun.* **2014**, *185*, 604−613.

DOI: 10.1021/acsnano.8b02856
ACS Nano 2018, 12, 8029−8036